Focusing Acoustic Beams with a Ball-Shaped Lens beyond the Diffraction Limit

J. H. Lopes,[1] M. A. B. Andrade,[2] J. P. Leão-Neto,[3] J. C. Adamowski,[4] I. V. Minin,[5] and G. T. Silva[3,*]

[1]*Grupo de Física da Matéria Condensada, Núcleo de Ciências Exatas, Universidade Federal de Alagoas, Arapiraca, Alagoas 57309-005, Brazil*

[2]*Institute of Physics, University of São Paulo, São Paulo, São Paulo 05314-970, Brazil*

[3]*Physical Acoustics Group, Instituto de Física, Universidade Federal de Alagoas, Maceió, Alagoas 57072-970, Brazil*

[4]*Department of Mechatronics and Mechanical Systems Engineering, University of São Paulo, São Paulo, São Paulo 05508-030, Brazil*

[5]*National Research Tomsk Polytechnic University, Tomsk, 30, Lenin Avenue, Russia, 634050*

(Received 31 March 2017; revised manuscript received 5 June 2017; published 18 August 2017; corrected 13 September 2017)

We report on measurements of a subwavelength focusing of an ultrasound beam by a polymer ball-shaped lens (Rexolite) immersed in water at room temperature. The beam arises in the near field of the ball-lens shadow side. Considering a 8.2λ-diameter ball lens, with λ being the wavelength, we find a superfocused beam with 14.4-dB-intensity gain, a full width and a full length at half maximum of $\lambda/2$ and 2.2λ, respectively, and sidelobes under -10 dB. The observed phenomenon is in excellent agreement with the theoretical and computational predictions based on the partial-wave expansion and finite-element methods. Our results may foster the design of simple lens elements for super-resolution acoustic microscopy and ultrasound imaging.

DOI: 10.1103/PhysRevApplied.8.024013

I. INTRODUCTION

Acoustic beam focusing on a subwavelength scale, i.e., where resolution is beyond the diffraction limit, has attracted great attention in recent decades. In this limit, an acoustic beam is referred to as a superfocused beam. Subwavelength focusing can markedly enhance the capabilities of ultrasound imaging for biomedical applications and nondestructive testing, underwater sonar, and acoustic microscopy. Also, it may further improve the ability to tweeze particles with the acoustic radiation force.

Acoustic superfocusing has been accomplished by some groundbreaking beam-forming methods. In acoustic microscopy, a resolution improvement beyond the diffraction limit by a factor of 1.4 using nonlinear harmonic generation was reported [1]. Nevertheless, doubling the frequency implies an increase of ultrasound absorption in liquids by a factor of 4. Based on ultrasound difference-frequency generation, it is possible to focus a beam in a subwavelength spot [2]. However, this is a very low-efficiency process, where only a small fraction of the input power produces the difference-frequency signal [3]. Another superfocusing method employs time-reversal mirrors to obtain a focal spot of $\lambda/14$ [4]. These mirrors are usually based on intense signal-processing methods for acquisition and time-reversal operations. Engineered superlenses with a negative index of refraction can also attain subwavelength focusing [5]. For instance, a phononic crystal operating as a superlens has been used to produce a subwavelength spot with a diameter of 0.74λ [6]. An acoustic magnifying hyperlens, made of a nonresonant radially symmetric layered structure, has reached a superfocusing of $\lambda/6.8$ [7]. Using a 2D array of Helmholtz resonators, it is possible to focus an acoustic beam in air on a spot as small as $\lambda/25$ [8]. Also, employing an engineered 3D holey-structured metamaterial, a superfocused acoustic beam with a feature size of $\lambda/50$ was obtained [9].

Despite outstanding advancements achieved by the aforementioned methods, they all have different levels of complexity involving either an intense signal-processing or (meta)material engineering. To find applications in the current technology of ultrasound imaging and acoustic microscopy, a superfocusing technique has to be scalable while adding a control hardware as simple as possible. Desirably, it should also allow real-time processed images.

Here, we experimentally show that a polymer sphere (a ball lens) can superfocus an acoustic beam beyond the diffraction limit on the near field of the sphere shadow region. The superfocused beam propagates over a few wavelengths without significant diffraction. Our theoretical analysis reveals that the beam is formed with the lens radius ranging from few to many wavelengths. A similar phenomenon happens in the electromagnetic scattering by a dielectric sphere or cylinder [10]. Subsequently, the term "photonic nanojet" was coined to describe this effect in the light scattering by a nanoparticle [11]. It is important to note that regular focusing effects in the sound scattering by a large spherical balloon filled with carbon dioxide were discussed in Refs. [12,13]. Moreover, a preliminary theoretical investigation of ball-lens focusing was presented by

*glauber@pq.cnpq.br

our group in Refs. [14,15]. In the experimental setup, we consider a rexolite ball lens of 8.2λ diameter operating at 1.01 MHz in water. The obtained superfocused ultrasound beam has 14.4-dB-intensity gain, focal spot with a full width and a full length at half maximum of $\lambda/2$ and 2.2λ, respectively, and sidelobes under -10 dB.

II. BALL-LENS FOCUSING THEORY

We assume that a traveling plane wave of angular frequency ω propagates along the z axis in a nonfriction fluid with density ρ_0 and adiabatic speed of sound c_0. The corresponding pressure amplitude is expressed as

$$p_{\text{in}} = p_0 e^{ikz}, \tag{1}$$

where i is the imaginary unit, $k = 2\pi/\lambda = \omega/c_0$ is the wave number, and p_0 is the pressure magnitude. The time-harmonic dependence $e^{-i\omega t}$ is omitted for simplicity. A sphere (ball lens) of radius a and density ρ_1 is placed in the wave path. As a result, the incident wave is scattered. We set the origin of the coordinate system in the ball-lens center. Owing to the symmetry of the problem, we describe the scattering pressure as a function of spherical coordinates: radial distance r to the observation point $\boldsymbol{r} = (x, y, z)$ and polar θ and azimuthal φ angles. The scattering problem as well as the experimental setup used to detect the superfocused ultrasound beam is shown in Fig. 1. The partial-wave expansion (PWE) method expresses the scattering pressure as

$$p_{\text{sc}}(kr, \theta) = p_0 \sum_{n=0}^{\infty} i^n (2n+1) s_n h_n^{(1)}(kr) P_n(\cos\theta), \tag{2}$$

where s_n is the scattering coefficient, $h_n^{(1)}$ and P_n are, respectively, the spherical Hankel function of first type and the Legendre polynomial of nth order.

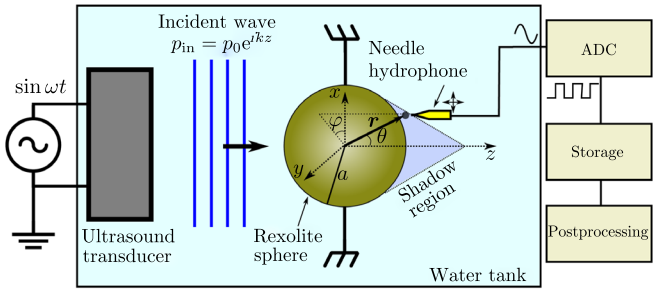

FIG. 1. The experimental setup used to measure the superfocused ultrasound beam in a water tank. A flat circular transducer generates an ultrasound beam which is scattered by a fixed Rexolite ball lens of radius a. A needle hydrophone is raster scanned to measure the pressure in the near field of the lens shadow region. The detected signal is digitized by an analog-to-digital converter (ADC), stored, and postprocessed in a computer.

The transmitted wave into the polymer ball lens is described by the displacement vector $\boldsymbol{u}$. Under small deformations, the mechanical behavior of a viscoelastic solid is assumed to be in accordance with Hooke's law [16],

$$\boldsymbol{\sigma} = \lambda_1(\omega)\nabla\cdot\boldsymbol{u} + \mu_1(\omega)(\nabla\boldsymbol{u} + \nabla\boldsymbol{u}^T), \tag{3}$$

where λ_1 and μ_1 are the complex Lamé functions. Elastic solids support waves with both longitudinal and shear modes. The corresponding dispersion relation of each mode is given by [16]

$$k_L^2 = \frac{\omega^2\rho_1}{\lambda_1(\omega) + 2\mu_1(\omega)}, \tag{4a}$$

$$k_S^2 = \frac{\omega^2\rho_1}{\mu_1(\omega)}. \tag{4b}$$

The real part of the Lamé functions corresponds to the material elasticity, which does not depend on the frequency. The imaginary part is related to the material viscous property. Hence, we rewrite the Lamé functions as

$$\lambda_1^* = \lambda_E + i\lambda_V(\omega), \tag{5a}$$

$$\mu_1^* = \mu_E + i\mu_V(\omega), \tag{5b}$$

where the asterisks denote complex conjugation. The longitudinal and shear speed of sound inside the ball lens are given by

$$c_L = \sqrt{\frac{\lambda_E + 2\mu_E}{\rho_1}}, \tag{6a}$$

$$c_S = \sqrt{\frac{\mu_E}{\rho_1}}. \tag{6b}$$

We defined the dimensionless absorption functions

$$\alpha_L(\omega) = \frac{\lambda_V(\omega) + 2\mu_V(\omega)}{2\rho_1 c_L^2}, \tag{7a}$$

$$\alpha_S(\omega) = \frac{\mu_V(\omega)}{2\rho_1 c_S^2}. \tag{7b}$$

After Taylor expanding (4) in the weak-absorption approximation $\alpha_L, \alpha_S \ll 1$, we encounter

$$k_L = \frac{\omega}{c_L}[1 + i\alpha_L(\omega)], \tag{8a}$$

$$k_S = \frac{\omega}{c_S}[1 + i\alpha_S(\omega)]. \tag{8b}$$

We adopt the hysteresis absorption model [17] in which α_L and α_S are not frequency dependent. This model is chosen because it accurately describes absorption in polymers.

The scattering coefficients s_n are obtained by solving the system of linear equations derived from the boundary conditions on the ball-lens surface [16]: the inner radial stress should be equalized to the external pressure, the inner solid and outer fluid displacements should be equal, and the tangential stresses should vanish. Accordingly, the scattering coefficient is given by

$$s_n = \det\begin{bmatrix} e_1 & d_{12} & d_{13} \\ e_2 & d_{22} & d_{23} \\ 0 & d_{32} & d_{33} \end{bmatrix} \det\begin{bmatrix} d_{11} & d_{12} & d_{13} \\ d_{21} & d_{22} & d_{23} \\ 0 & d_{32} & d_{33} \end{bmatrix}^{-1}. \quad (9)$$

The matrix elements e_1, e_2, and d_{ij} (with $i, j = 1, 2, 3$) are given in Appendix B of Ref. [16].

The superfocused ultrasound beam will be described by the time-averaged acoustic intensity of the scattered wave. In turn, the instantaneous intensity is given as a product of pressure and fluid velocity [Eq. (3.276) of Ref. [18]]. Thus, consider the time average of the product of two harmonic functions, $f_1 e^{-i\omega t}$ and $f_2 e^{-i\omega t}$, over the period $2\pi/\omega$ as

$$\overline{f_1 e^{-i\omega t} f_2 e^{-i\omega t}} = \frac{1}{2}\mathrm{Re}[f_1 f_2^*], \quad (10)$$

where Re represents the real part of a function. The time average of the axial intensity outside the ball lens and normalized to the plane-wave intensity $I_0 = p_0^2/2\rho_0 c_0$ is expressed by

$$I_z = \frac{1}{2I_0}\mathrm{Re}[(p_{\mathrm{in}} + p_{\mathrm{sc}})(v_{\mathrm{in},z}^* + v_{\mathrm{sc},z}^*)], \quad (11)$$

with

$$v_{\mathrm{in(sc)},z} = -\frac{i}{\rho_0 c_0 k}\partial_z p_{\mathrm{in(sc)}} \quad (12)$$

being the incident (scattered) fluid-element velocity along the z direction. Henceforth, the normalized intensity averaged in time will be referred to as intensity. In our analysis, we find that the transverse components of the intensity (I_x, I_y) contribute to less than $1/50$ to the intensity magnitude $I = \sqrt{I_x^2 + I_y^2 + I_z^2}$. Hence, we shall not consider transverse components here. Moreover, the focusing gain is defined as

$$G[\mathrm{dB}] = 10\log I_z. \quad (13)$$

We are also interested in the axial intensity transmitted into the ball lens [Eq. (3.289) of Ref. [18]],

$$I_{\mathrm{tr},z} = -\frac{1}{2I_0}\mathrm{Re}[i\omega \boldsymbol{u}^* \cdot \boldsymbol{\sigma}] \cdot \boldsymbol{e}_z, \quad (14)$$

where $\boldsymbol{e}_z$ is the axial unit vector and the centered dot indicates the scalar product.

Our analysis is carried out with regard to the descriptive parameters of ultrasound beams, namely, peak intensity (or gain) and its axial position, full width at half maximum (FWHM), and full length at half maximum (FLHM). The FWHM and FLHM are, respectively, the width and the length of the beam intensity at -3 dB (Chap. 3 of Ref. [19]). Consider an ultrasound beam generated by an aperture b and focused at z_0 along the axial direction. In the paraxial approximation, $(z_0/b)^2 \ll 1$, the classical diffraction theory determines that the FWHM should satisfy [Eq. (3.3.14) of Ref. [19]]

$$\mathrm{FWHM} > \frac{1.22 z_0 \lambda}{b}. \quad (15)$$

This condition establishes the diffraction limit to which the FWHM cannot be smaller than one wavelength. The last descriptive parameter in our analysis is the focusing quality factor [20],

$$Q = \left(\frac{\mathrm{FLHM}}{\mathrm{FWHM}}\right) I_z. \quad (16)$$

If the intensity is high and the FWHM is small, Q is large.

Now we theoretically study the characteristics of a superfocused beam generated by a Rexolite ball lens in water at room temperature; see the physical parameters in Table I. Rexolite is chosen due to its good acoustic

TABLE I. Physical parameters of the ball lens and the host medium at room temperature.

Description	Value
Medium: water [21]	
Density (ρ_0)	998 kg m^{-3}
Speed of sound (c_0)	1493 m s^{-1}
Ball lens: Rexolite 1422 [22]	
Radius (a)	12.2 cm
Density (ρ_1)	1049 kg m^{-3}
Longitudinal speed of sound (c_L)	2337 m s^{-1}
Shear speed of sound (c_S)	1157 m s^{-1}
Longitudinal absorption coefficient (α_L)	0.0028
Shear absorption coefficient (α_S)	0.0037

properties, i.e., low attenuation and specific acoustic impedance relatively close to water.

The descriptive parameters are computed from the intensity in Eq. (11), which is evaluated with Eqs. (1) and (2). The lens size parameter ka ranges in the interval $4\pi \leq ka < 80\pi$. Hence, we cover from the Mie ($ka \sim 1$) to the geometrical ($ka \gg 1$) scattering regimes. A word should be said about numerically computing Eq. (2). To ensure a proper convergence of the partial-wave series, we truncate it at $N = ka + 4.05(ka)^{1/3} + 2$, following Wiscombe's criterion [23].

In Fig. 2(a), we plot the FWHM and FLHM as a function of the ball-lens radius. We observe that the superfocused beam is formed in the entire range where the FWHM is smaller than 0.7λ. The FLHM increases with radius. In Fig. 2(b), we show the peak intensity and its axial position (measured away from the lens surface) versus radius a. The peak intensity reaches its maximum value at $a = 19\lambda$ with gain $G = 20\,\mathrm{dB}$. The observed intensity decaying is caused by absorption inside the ball lens. Furthermore, a fluctuation pattern is noted, which is likely to be caused by diffraction effects inside the lens. Nevertheless, the peak position moves away from the lens as the radius increases.

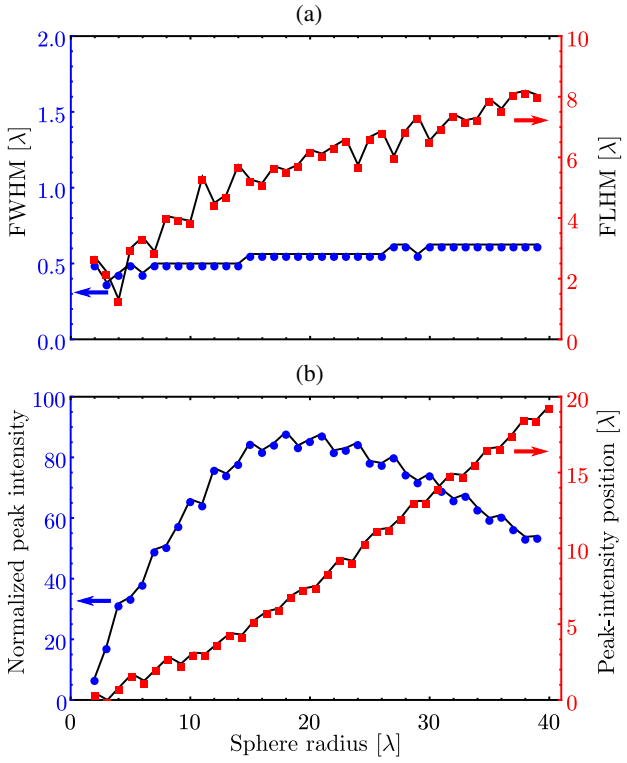

FIG. 2. Descriptive parameters of the superfocused beam versus the lens radius for (a) FWHM and FLHM, and (b) peak-intensity and its axial position. The left and right vertical axes are related, respectively, to the blue-dot and red-square markers. The intensity is obtained by numerically computing Eqs. (2) and (11).

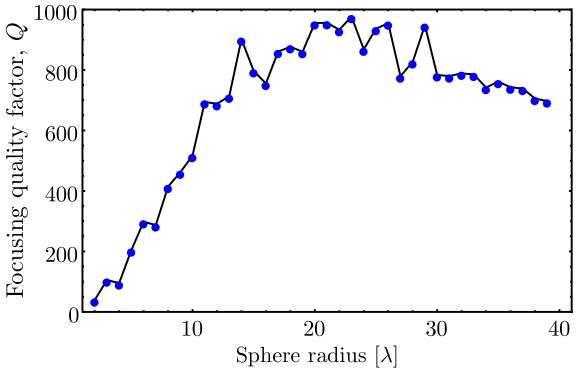

FIG. 3. Focusing quality factor (Q) versus the lens radius. The Q factor is computed using Eq. (16).

The quality factor (Q) is illustrated in Fig. 3. We observe that the highest Q factor is 976.5, which occurs at $a = 23\lambda$. Around this radius, the Q factor exhibits fluctuations. Moreover, we notice that the Q factor decreases for $a > 30\lambda$.

III. EXPERIMENTAL RESULTS

We proceed to explain the experimental apparatus used to detect the superfocused beam in a water tank, as shown in Fig. 1. An ultrasound wave is generated by a 25-mm-diameter flat transducer. A 1.01-MHz pure tone is produced by a function generator and is subsequently amplified to drive the transducer with a rf amplifier. The wavelength is $\lambda = 1.48$ mm. A homemade Rexolite ball lens with a 12.2-mm diameter (8.28λ) is suspended by a thin string and placed along the transducer central axis, 700 mm from its face. This distance is chosen to ensure that the incident wave is nearly a traveling plane wave. The acoustic pressure field in the ball-lens shadow zone is measured by raster scanning a 0.2-mm-diameter (approximately $\lambda/8$) hydrophone with transverse and axial steps of 0.2 and 0.4 mm (about $\lambda/8$ and $\lambda/4$), respectively. The detected signals are digitized by an analog-to-digital converter at 100 megasamples/s and postprocessed to obtain the magnitude and phase of pressure for each scanned point. The scattering intensity is computed using *Mathematica* (Wolfram Research, Inc., Champaign, Illinois).

In Fig. 4, we show the results for the PWE and finite-element (FE) methods, and the measured superfocused beam for a Rexolite ball lens with radius $a = 4.14\lambda$ in water. The FE method is implemented in COMSOL Multiphysics (Comsol, Inc., Burlington, Massachusetts) with a mesh having ten points per wavelength. We present in Fig. 4(a) a comparison between the intensity (in the axial direction) obtained by the PWE and FE methods with the experimental data.

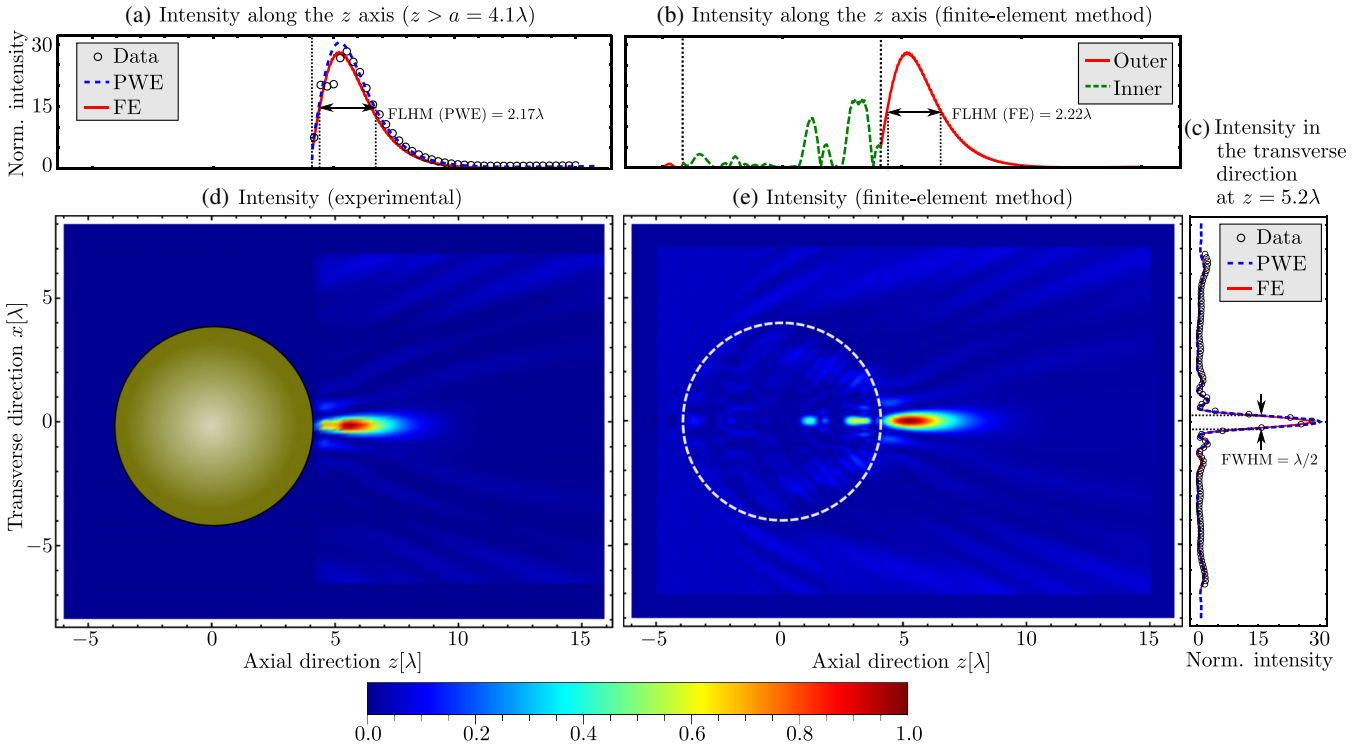

FIG. 4. Comparison of the partial-wave expansion (PWE) and finite-element (FE) methods with experimental data of the superfocused beam by a Rexolite ball lens with radius $a = 4.14\lambda$ in water. (a) The intensity along the z direction with $z > a$. (b) The FE results for the inner and outer intensities along the z direction. (c) The intensity along the transverse direction at $z = 5.2\lambda$. (d) The experimental result for the superfocused beam intensity in the x-z plane. Here, the measured pressure is used in Eq. (11) to compute the intensity. (e) The FE result for the superfocused beam showing the inner and outer intensities in the x-z plane. A white-dashed circle depicts the ball lens. In (d) and (e), the intensities are normalized to 28.2, i.e., the peak intensity computed by the FE method.

In Fig. 4(b), we show both the transmitted and scattering intensities computed by the FE method along the z axis. A comparison of the intensity along the transverse direction is shown in Fig. 4(c). Clearly, the diffraction limit is overcome by the ultrasound beam. Figures 4(d) and 4(e) display, respectively, the experimental and FE-computed intensities in the x-z plane. To allow visual comparison, the intensities are normalized to the maximum value obtained by the FE method, $\max\{I_{\mathrm{sc}}^{\mathrm{FE}}\} = 28.2$. See also the Video 1 animation of the superfocused ultrasound pressure in the x-z plane. We note in Fig. 4(e) that the inner intensity $I_{\mathrm{tr},z}$ is focused toward the shadow region of the ball lens.

To quantify the difference between the observed data and the theoretical predictions, we use the root-mean-squared (rms) error normalized to the observed data 27.6. The descriptive focusing parameters and the normalized rms (nrms) error are summarized in Table II. The quality factor and gain of the measured superfocused beam are $Q = 121.4$ and $G = 14.4$ dB, respectively. The sidelobes are under -10 dB. We find excellent agreement between theory, computational simulations, and experimental data; see Table II. The similarities between Figs. 4(d) and 4(e) are particularly striking.

We illustrate the time variation of the focused pressure by the ball lens in Video 1. Clearly, the focused beam behaves as a traveling wave. Moreover, an excellent agreement between the numerical and experimental animations is noted.

TABLE II. Descriptive parameters for the superfocused beam explained in the caption of Fig. 4, and the normalized rms (nrms) error between predicted and experimental data.

	Descriptive parameters			nrms error	
Method	Peak intensity	FWHM	FLHM	Axial	Transverse
FE	28.2	$\lambda/2$	2.22λ	5.8%	1.45%
PWE	30.1	$\lambda/2$	2.17λ	6.8%	1.73%
Experimental data	27.6	$\lambda/2$	2.20λ	⋯	⋯

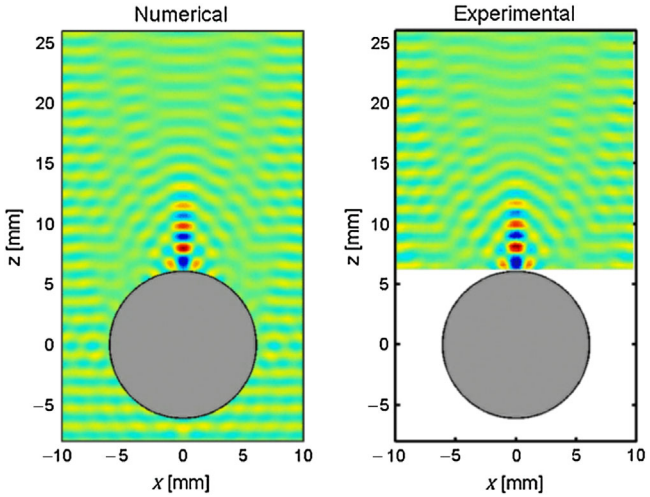

VIDEO 1. Time variation of the pressure field focused by the Rexolite ball lens with radius $a = 4.14\lambda$ in water.

IV. DISCUSSION AND CONCLUSIONS

Superfocused beams are formed from the Mie ($ka \sim 1$) to the geometrical ($ka \gg 1$) scattering regimes. Larger ball lenses tend to produced less-intense beams because internal absorption takes its toll. Low-absorptive materials should be sought to avoid attenuation. In general, metal spheres have low absorption. We have found that some metal ball lenses (stainless steel, brass, and tungsten carbide) may also produce superfocused beams. However, because of an acute impedance mismatch, the intensity is low compared to that of a polymer material. Therefore, polymer ball lenses with low attenuation seem to be more suited to work as superlenses. Currently, we are investigating the feasibility of superfocusing with a core-shell lens with a liquid core and a polymer coating layer.

Finally, our experiment demonstrates that a solid sphere can be used as a superlens for acoustic beams. Given the design simplicity, our findings may have a great impact on the physics of ultrasound and its applications. The ball superlenses can be readily adapted to ultrasound imaging systems, as well as acoustic microscopy technology. They may also foster subwavelength particle manipulation based on the acoustic radiation force [24–26] and an alternative generation of acoustic sensors operating beyond the diffraction limit.

ACKNOWLEDGMENTS

This work was partially supported by the Brazilian agencies Conselho Nacional de Desenvolvimento Científico e Tecnológico-CNPq (Grant No. 307221/2016-4) and Fundação de Amparo à Pesquisa do Estado de Alagoas-FAPEAL (Grant No. 1024/2016). I. V. Minin was partially supported by Tomsk Polytechnic University Competitiveness Enhancement Program grant, Project No. TPU CEP_INDT_76\2017.

[1] D. Rugar, Resolution beyond the diffraction limit in the acoustic microscope: A nonlinear effect, J. Appl. Phys. **56**, 1338 (1984).
[2] M. Fatemi and J. F. Greenleaf, Ultrasound-stimulated vibro-acoustic spectrography, Science **280**, 82 (1998).
[3] G. T. Silva and F. G. Mitri, Difference-frequency generation in vibro-acoustography, Phys. Med. Biol. **56**, 5985 (2011).
[4] J. de Rosny and M. Fink, Overcoming the Diffraction Limit in Wave Physics Using a Time-Reversal Mirror and a Novel Acoustic Sink, Phys. Rev. Lett. **89**, 124301 (2002).
[5] J. B. Pendry, Negative Refraction Makes a Perfect Lens, Phys. Rev. Lett. **85**, 3966 (2000).
[6] A. Sukhovich, B. Merheb, K. Muralidharan, J. O. Vasseur, Y. Pennec, P. A. Deymier, and J. H. Page, Experimental and Theoretical Evidence for Subwavelength Imaging in Phononic Crystals, Phys. Rev. Lett. **102**, 154301 (2009).
[7] J. Li, L. Fok, X. Yin, G. Bartal, and X. Zhang, Experimental demonstration of an acoustic magnifying hyperlens, Nat. Mater. **8**, 931 (2009).
[8] F. Lemoult, M. Fink, and G. Lerosey, Acoustic Resonators for Far-Field Control of Sound on a Subwavelength Scale, Phys. Rev. Lett. **107**, 064301 (2011).
[9] J. Zhu, J. Christensen, J. Jung, L. Martin-Moreno, X. Yin, L. Fok, X. Zhang, and F. J. Garcia-Vidal, A holey-structured metamaterial for acoustic deep-subwavelength imaging, Nat. Commun. **7**, 52 (2011).
[10] D. S. Benincasa, P. W. Barber, J.-Z. Zhang, W.-F. Hsieh, and R. K. Chang, Spatial distribution of the internal and near-field intensities of large cylindrical and spherical scatterers, Appl. Opt. **26**, 1348 (1987).
[11] Z. Chen and A. Taflove, Photonic nanojet enhancement of backscattering of light by nanoparticles: A potential novel visible-light ultramicroscopy technique, Opt. Express **12**, 1214 (2004).
[12] D. C. Thomas, K. L. Gee, and R. S. Turley, A balloon lens: Acoustic scattering from a penetrable sphere, Am. J. Phys. **77**, 197 (2009).
[13] M. A. P. Borrero, M. Prez-Saborid, and J. M. F. Garca, Acoustic scattering from a spherical lens irradiated by a finite transducer: Focusing effect and refraction, Am. J. Phys. **79**, 401 (2011).
[14] J. H. Lopes, J. P. Leão-Neto, I. V. Minin, O. V. Minin, and G. T. Silva, in *Proceedings of the 22nd International Congress on Acoustics (ICA 2016), Buenos Aires, 2016*, www.ica2016.org.ar/ica2016proceedings/ica2016/ICA2016-0943.pdf.
[15] O. V. Minin and I. V. Minin, Acoustojet: Acoustic analogue of photonic jet phenomenon based on penetrable 3D particle, Opt. Quantum Electron. **49**, 54 (2017).
[16] J. P. Leão-Neto and G. T. Silva, Acoustic radiation force and torque exerted on a small viscoelastic particle in an ideal fluid, Ultrasonics **71**, 1 (2016).
[17] B. Hartmann and J. Jarzynski, Ultrasonic hysteresis absorption in polymers, J. Appl. Phys. **43**, 4304 (1972).
[18] A. D. Pierce, in *Springer Handbook of Acoustics*, edited by T. D. Rossing (Springer Science+Business Media, New York, 2007), Chap. 3, pp. 29–115.
[19] G. S. Kino, *Acoustic Waves: Devices, Imaging and Analog Signal Processing* (Prentice-Hall, Englewood Cliffs, NJ, 1987).

[20] C. Liu, Ultra-elongated photonic nanojets generated by a grade-index microellipsoid, Prog. Electromagn. Res. Lett. **37**, 153 (2013).

[21] *CRC Handbook of Chemistry and Physics*, 85th ed., edited by D. R. Lide (CRC Press, Boca Raton, 2005).

[22] C. Cadot, J.-F. Saillant, and B. Dulmet, in *Proceedings of the 19th World Conference on Non-Destructive Testing 2016, Munich, 2016*, http://ndt.net/?id=19542.

[23] W. J. Wiscombe, Improved Mie scattering algorithms, Appl. Opt. **19**, 1505 (1980).

[24] G. T. Silva, Acoustic radiation force and torque on an absorbing compressible particle in an inviscid fluid, J. Acoust. Soc. Am. **136**, 2405 (2014).

[25] G. T. Silva and H. Bruus, Acoustic interaction forces between small particles in an ideal fluid, Phys. Rev. E **90**, 063007 (2014).

[26] G. T. Silva and A. L. Baggio, Designing single-beam multitrapping acoustical tweezers, Ultrasonics **56**, 449 (2015).